Supporting Information

20% STH in solar driven water electrolysis by endowing charge transfer path between LDH layers and optimizing oxygen absorption state in noble-metal free NiFe- LDH electrodes

Yan Li,[a, b] Gongxuan Lu*[a]

[a] State Key Laboratory of Low Carbon Catalysis and Carbon Dioxide Utilization, Lanzhou Institute of Chemical Physics, Chinese Academy of Sciences, Lanzhou 730000, China

[b] University of Chinese Academy of Sciences, Beijing 100049, China

*Corresponding authors.

E-mail addresses: gxlu@lzb.ac.cn (G. Lu)

1. Experimental Section

1.1. Materials

All chemicals were commercial purchased and used without further purification. Nickel nitrate ($Ni(NO_3)_2·6H_2O$, Xilong Chemical Co., Ltd, AR, ≥98.0%), ferric nitrate ($Fe(NO_3)_3·9H_2O$, Chengdu Cologne Chemicals Co., LtD, AR, ≥98.5%), urea (CH_4N_2O, Chengdu Cologne Chemicals Co., LtD, AR, ≥99.0%), Sodium sulfide ($Na_2S·9H_2O$, Shanghai Macklin Biochemical Co., Ltd, AR, ≥98.0%), potassium hydroxide (KOH, Xilong Chemical Co., Ltd, AR, ≥85.0%), ethyl alcohol (CH_3CH_2OH, Lianlong Bohua Pharmaceutical Chemistry Co., Ltd, AR, ≥99.7%), isopropanol ($(CH_3)_2CHOH$, Lianlong Bohua Pharmaceutical Chemistry Co., Ltd, AR, ≥99.7%), hydrochloric acid (HCl, Xilong Chemical Co., Ltd, AR, 36.0-38.0%).

1.2. Preparation of NiFe-LDH-NFs

Nickel foams (NFs) substrates (2.5 × 3 cm) were cleaned by ultrasound with 6 mol L^{-1} HCl, deionized (DI) water and anhydrous ethanol for 15 min, followed by vacuum drying at 60 ℃ for 5 h. An aqueous precursor solution was prepared by dissolving 0.516 mmol $Ni(NO_3)_2$ $6H_2O$, 0.557 mmol $Fe(NO_3)_3$ $9H_2O$, and 2.498 mmol CH_4N_2O in 30 mL DI water. The cleaned NFs were then immersed in the homogeneous solution within a 50 mL Teflon-lined autoclave, which was subsequently sealed and maintained at 120 °C for 12 h.

1.3. Preparation of NiFe-S^{2-}-LDH-NFs

The prepared NiFe-LDH-NFs catalyst was subjected to anion exchange in 30 mL of 0.1 M Na_2S solution under argon atmosphere for 6 hours, yielding the NiFe-S^{2-}-LDH- NFs. In addition, a series of S^{2-} intercalation samples were prepared using Na_2S solutions with varying concentrations (0.01, 0.05, 0.3, and 0.5 M), maintaining otherwise identical reaction conditions.

1.4. Preparation of NiFeS_x-LDH-NFs

The S^{2-} intercalated NiFe-S^{2-}-LDH-NFS catalyst prepared by anion exchange, along with 30 mL Na_2S solution of five concentrations (0.01, 0.05, 0.1, 0.3, 0.5 M), were placed in the Teflon-lined autoclave. Subsequent hydrothermal treatment at different temperatures (80, 100, 120, and 140 ℃) for 6 hours yielded the corresponding NiFeS_x-LDH-NFs materials.

1.5. Preparation of Pt/C-NFs

The benchmark Pt/C electrode was prepared by dispersing 3 mg of commercial 20 wt% Pt/C in 950 μL isopropanol/water (7/3) solution and 50 μL Nafion solution, followed by sonication for 30 min to form a homogeneous ink. The resulting dispersion was then drop-cast onto a NF substrate (1 cm^2) and air-dried at room temperature, yielding a Pt/C-NF electrode with a catalyst loading of 3 mg cm^{-2}.

1.6. Preparation of RuO_2-NFs

Prepared analogously to Pt/C-NFs but using RuO_2 instead.

1.7. Electrochemical measurements

The electrochemical tests were performed using a Shanghai Chen Hua (CHI 660E) electrochemical workstation with a three-electrode system at room temperature; the prepared $NiFeS_x$-LDH-NFs electrode was used as the working electrode, the Ag/AgCl electrode (0.3 mol L^{-1} KCl) as the reference electrode, the graphite rod as the counter electrode, and 1 M KOH solution as the electrolyte. Linear sweep voltammetry (LSV) curves were recorded with a scan rate of 2 mV s^{-1}. Electrochemical active surface area (ECSA) of HER was tested in range of 0.1-0.2 V vs RHE at scan rates of 20, 40, 60, 80, 100, and 120 mV s^{-1}; and the ECSA of OER was tested in the range of 1.0-1.1 V vs RHE at scan rates of 20, 40, 60, 80, 100, and 120 mV s^{-1}, respectively. And electrochemical impedance spectroscopy (EIS) was performed by applying different voltages in the frequency range of 0.01 to 106 Hz. All potentials were converted to the standard reversible hydrogen electrode (RHE) potential using the Equation: $E_{RHE} = E_{Ag/AgCl} + 0.210 + 0.059 \times pH$.

1.8. Solar-to-hydrogen (STH) efficiencies calculations

Calculate the solar-to-hydrogen (STH) efficiencies by the equation $STH = \frac{R_{H_2}(umol/s)\times\Delta G_r(kJ/mol)}{P_{light}(mW/cm^2)\times S(cm^2)} \times 100\%$;

(1) $\boldsymbol{R_{H_2}}$ is the hydrogen precipitation rate of the water decomposition process, and this value is calculated as follows:

The volume of gas produced by the photovoltaic-electrolytic water system was recorded at intervals of 0.5 h (mL h^{-1}), then the volume of gas was converted into the amount of substance by the

formula PV = nRT, where P is the local (Chengguan District, Lanzhou City, Gansu Province, China) atmospheric pressure, which is roughly 85325 Pa; V is the recorded volume of gas produced multiplied by 2/3, (The "2/3" was obtained with an Agilent 6820 gas chromatograph. The photocatalytic water splitting produces hydrogen and oxygen in a 2:1 ratio, making hydrogen volume 2/3 of the total gas output); R is 8.314 J $mol^{-1} \cdot K^{-1}$; T is the daily measured temperature.

(2) ΔG_r is the Gibbs free energy required for water decomposition, ΔG_r = 237.2 kJ mol^{-1} at 298 K.

(3) P_{light} is the calibrated intensity of incident simulated sun (AM1.5G), and the incident simulated sun power was measured using a Newport 843-R economic portable power meter, which was calibrated prior to the experiment.

(4) S is the light absorption area, which is the light-sensitive area of the solar cell (0.25 cm^2).

1.9. Faraday efficiency (FE) calculation

The Faraday efficiency of hydrogen production through water splitting was calculated by comparing the theoretical charge transfer and actual charge consumption of the HER process by the formula FE = $\frac{n_{H_2}(mol) \times z \times F(C/mol)}{i(A/cm^2) \times t(s)} \times 100\%$.

Where, **n** is the amount of hydrogen produced during water splitting (mol), **z** is the number of electrons transferred by the HER reaction (2), **F** is Faraday's constant, 96485 C mol^{-1}, **i** is the average current density (A cm^{-2}), and **t** is the reaction time.

1.10. Characterization

The crystal structure of the catalysts was analyzed by an X-ray diffractometer (XRD) manufactured by Rigaku, Japan, using X-rays derived from copper Kα radiation, scanned in the 2θ range of 5-70°. The chemical composition and structure of the catalysts were analyzed by an ESCALAB 250Xi-XPS photoelectron spectrometer (Thermo Fisher Scientific, USA) with a monochromatic Al Kα (hυ = 1486.6 eV) radiation source, corrected for elemental binding energy using C1s (284.8 eV). Transmission electron microscopy (TEM) and high-resolution transmission electron microscopy (HRTEM) were characterized using a Tecnai-G2-TF20 transmission electron microscope

from FEI, with an electron beam operating voltage of 200 kV. The samples were sonicated so that a small amount of surface material fell off and was dispersed in anhydrous ethanol, the dispersed suspension was dropped onto a Cu grid and dried naturally and slowly to obtain the TEM test samples. Fourier transform infrared (FT-IR) spectra were acquired on a Nicolet Nexus 870 infrared spectrometer over a range of 400-4000 cm^{-1}. The Raman scattering was carried out using an argon ion laser at 20 mW (532 nm, Renishaw inVia Raman microscope). The morphology of the catalyst was characterized by a JSM-5601LV scanning electron microscope. Inductively coupled plasma spectrometer (ICP, Agilent 5110) was used to analysis the elemental content ratios of Ni and Fe in the catalyst. Aberration-corrected high-angle annular dark-field scanning transmission electron microscopy (AC-HAADF-STEM) images were obtained using a TFS-Spectra 300 microscope operated at 200 kV, under 1×10^{-5} Pa at 298 K in the sample column. X-ray absorption fine structure (XAFS) spectroscopy was carried out using the Table XAFS-500A (Specreation Instruments Co., Ltd.) by transmission mode at 20 mA, 20 kV (Fe) and 25 kV (Ni), and the Ge (620) and Si (551) spherically bent crystal analyzer with a radius of curvature of 500 mm was used for Fe and Ni, respectively.

1.11. Density functional theory (DFT) calculations

All density functional theory calculations in this study are performed by with the Vienna ab initio simulation package (VASP) [1]. The Perdew-Burke-Ernzerhof (PBE) [2] functional was employed to treat the exchange-correlation interactions. The plane-wave basis set with a kinetic energy cutoff of 400 eV, the energy convergence criterion of 10-5 eV, the force convergence criterion of 0.02 eV $Å^{-1}$, and a (2 × 2 × 1) Monkhorst-Pack k-point sampling were employed for structure relaxation. A sufficiently large vacuum gap (> 12 Å) was employed to prevent the interaction between neighboring periodic structures along the c-axis. H_2 and H_2O were calculated in boxes of 20 Å × 20 Å × 20 Å with the gamma point only. The free energy diagrams for OER were calculated with reference to the computational hydrogen electrode [3]. The free energy of the gas phase and adsorbed species can be obtained from the following equation:

$$\Delta G = \Delta E_{DFT} + \Delta ZPE - T\Delta S$$

where EDFT was the electronic energy, T was set at 298.15 K. ΔZPE and TΔS were the change in the zero point energy and entropy at room temperature (T = 298.15 K), which were obtained after

frequency calculations.

Generally, the proposed four-electron transfer mechanism of the OER process in alkaline electrolytes is based on the following multistep reactions:

$* + OH^- \rightarrow *OH + e^-$

$*OH + OH^- \rightarrow *O + H_2O + e^-$

$*O + OH^- \rightarrow *OOH + e^-$

$*OOH + OH^- \rightarrow * + O_2 + H_2O + e^-$

2. Supporting pictures

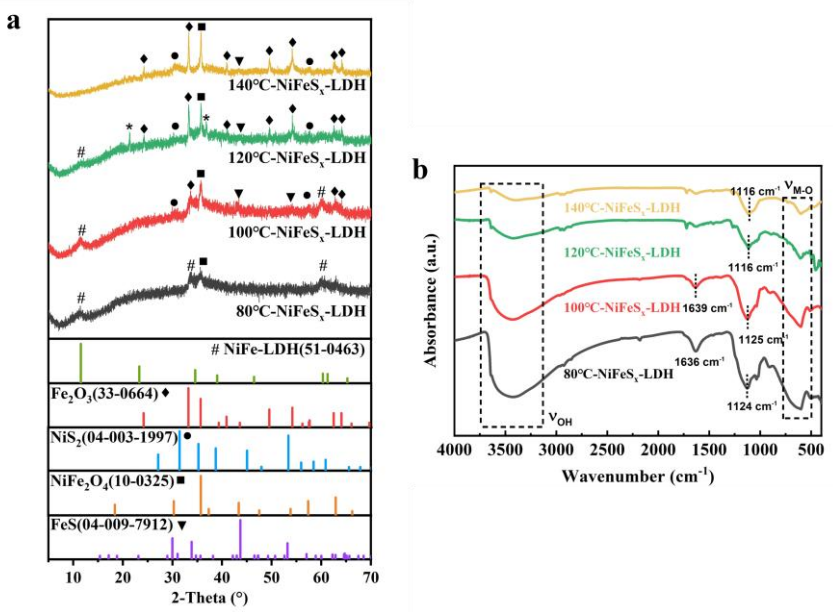

Fig. S1 (a) XRD patterns and (b) FT-IR spectra of 80 ℃-NiFeS$_x$-LDH-NFs, 100 ℃-NiFeS$_x$-LDH-NFs, 120 ℃-NiFeS$_x$-LDH-NFs, and 140 ℃-NiFeS$_x$-LDH-NFs.

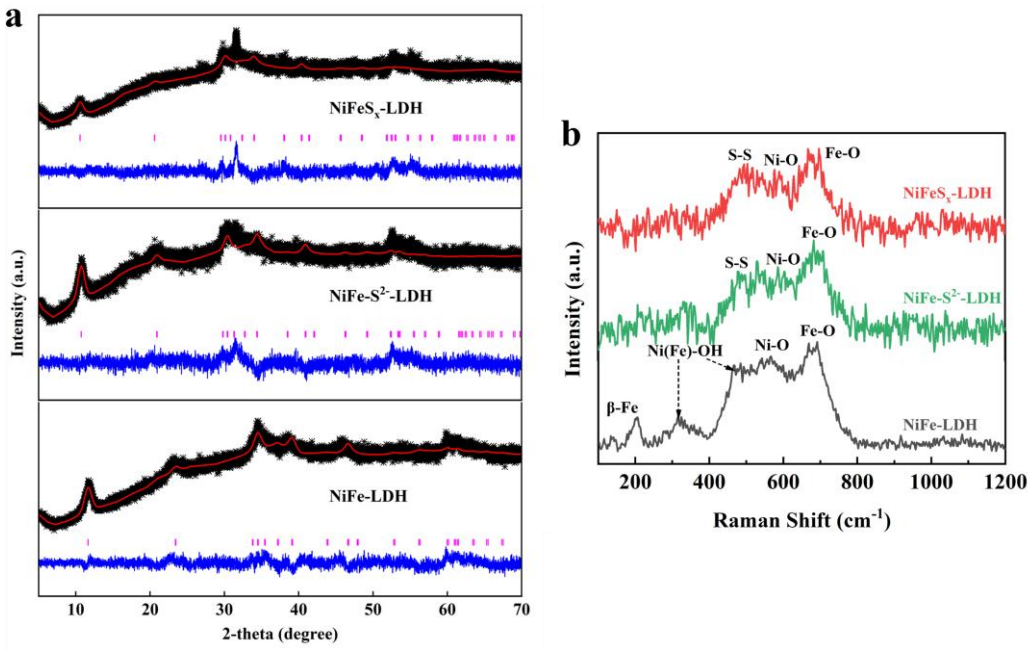

Fig. S2 Raman spectra of NiFe-LDH-NFs, NiFe-S^{2-}-LDH-NFs, and $NiFeS_x$-LDH-NFs.

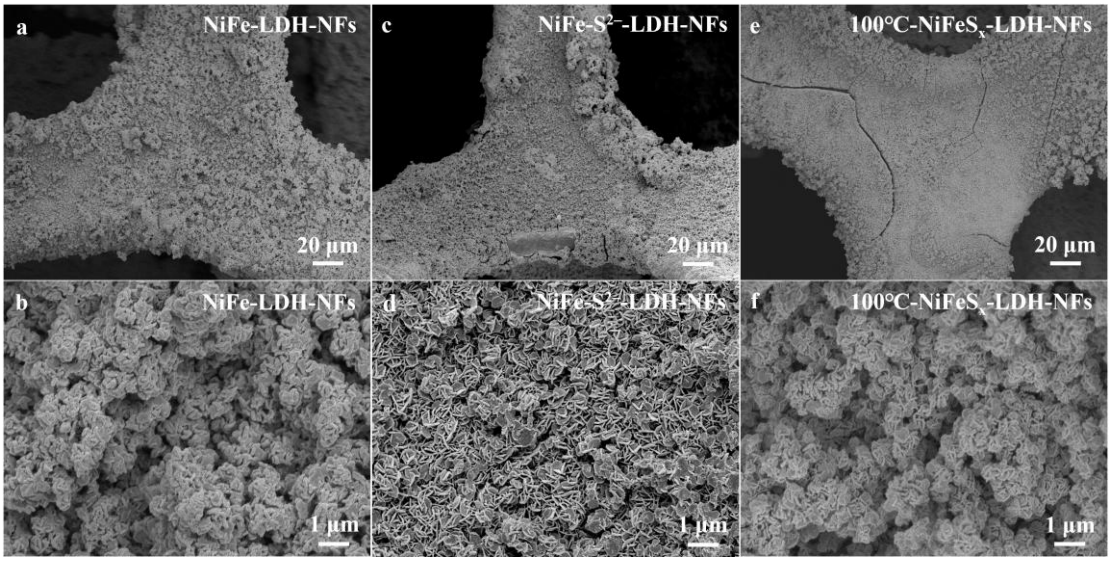

Fig. S3 Scanning electron microscope (SEM) images of (a, b) NiFe-LDH-NFs, (c, d) NiFe-S^{2-}-LDH-NFs, and (e, f) 100 ℃-$NiFeS_x$-LDH-NFs.

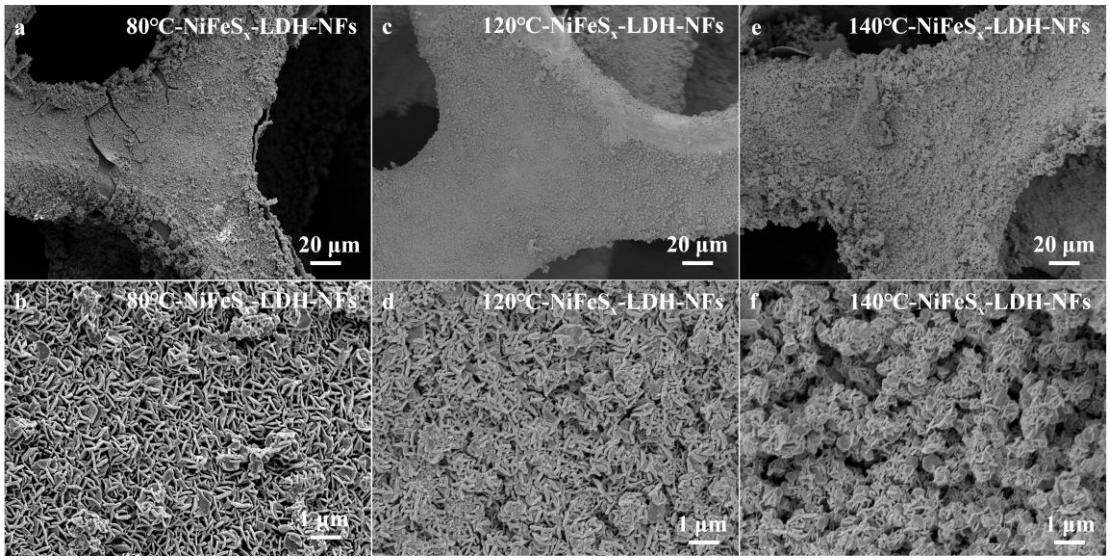

Fig. S4 Scanning electron microscope (SEM) images of (a, b) 80 ℃-$NiFeS_x$-LDH-NFs, (c, d) 120 ℃-$NiFeS_x$-LDH-NFs, and (e, f) 140 ℃-$NiFeS_x$-LDH-NFs.

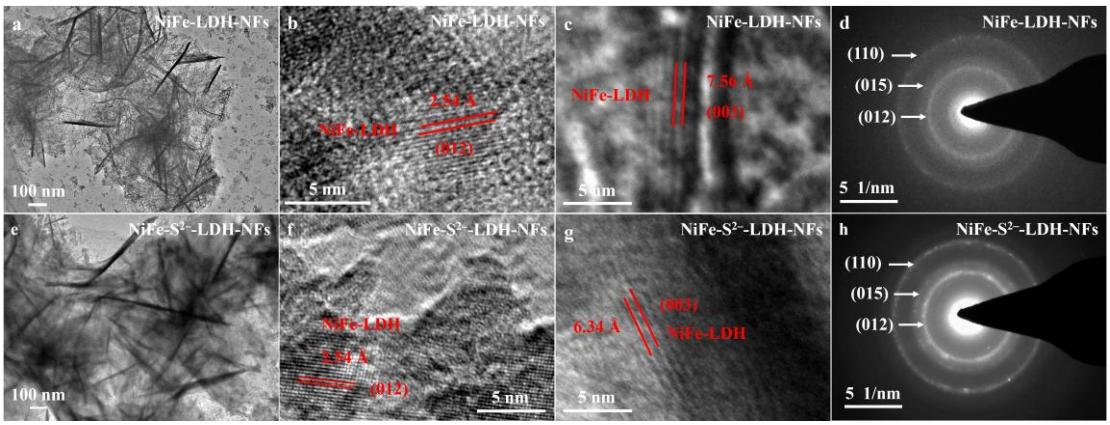

Fig. S5 (a) TEM, (b, c) HRTEM, and (d) the selected area electron diffraction images of NiFe-LDH-NFs, (e) TEM, (f, g) HRTEM, and (h) the selected area electron diffraction images of NiFe-S^{2-}-LDH-NFs.

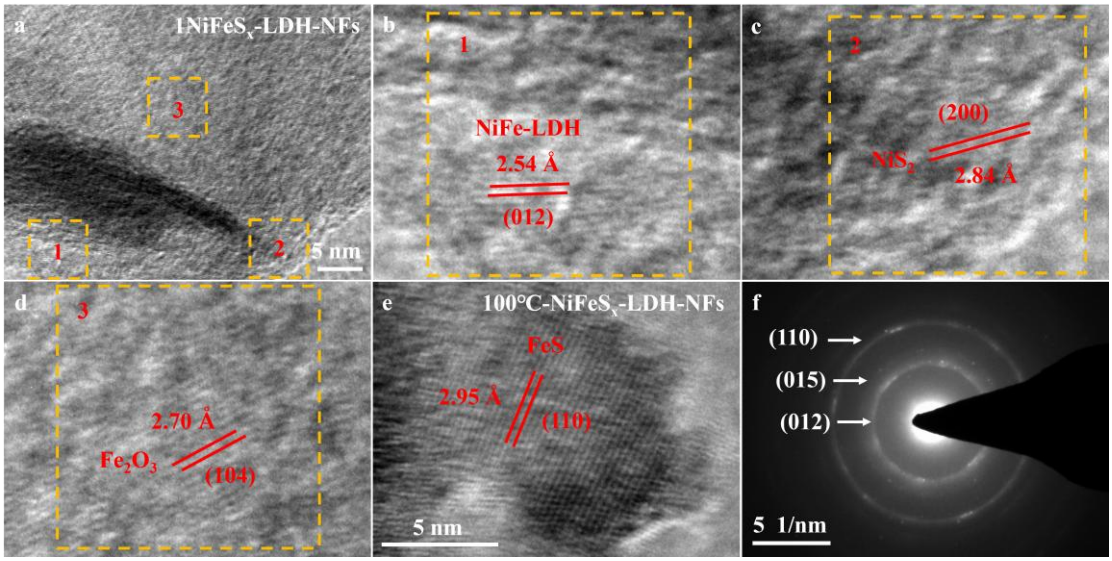

Fig. S6 (a-e) HRTEM and (f) the selected area electron diffraction images of $NiFeS_x$-LDH-NFs.

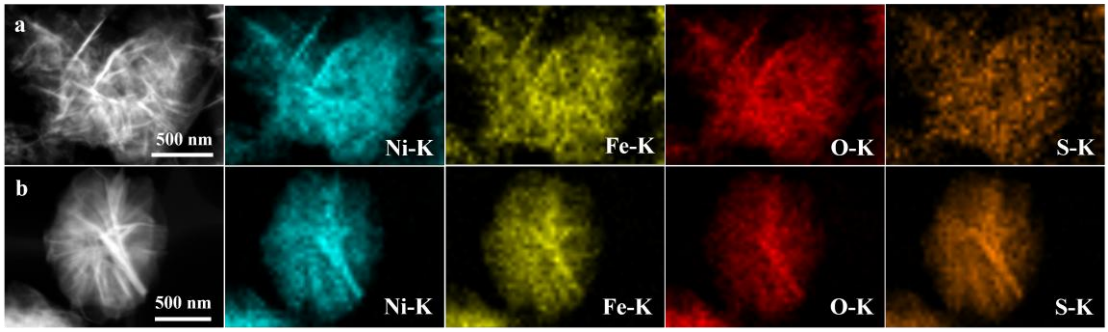

Fig. S7 (a) and (b) elemental mapping images of NiFe-S^{2-}-LDH-NFs and $NiFeS_x$-LDH-NF.

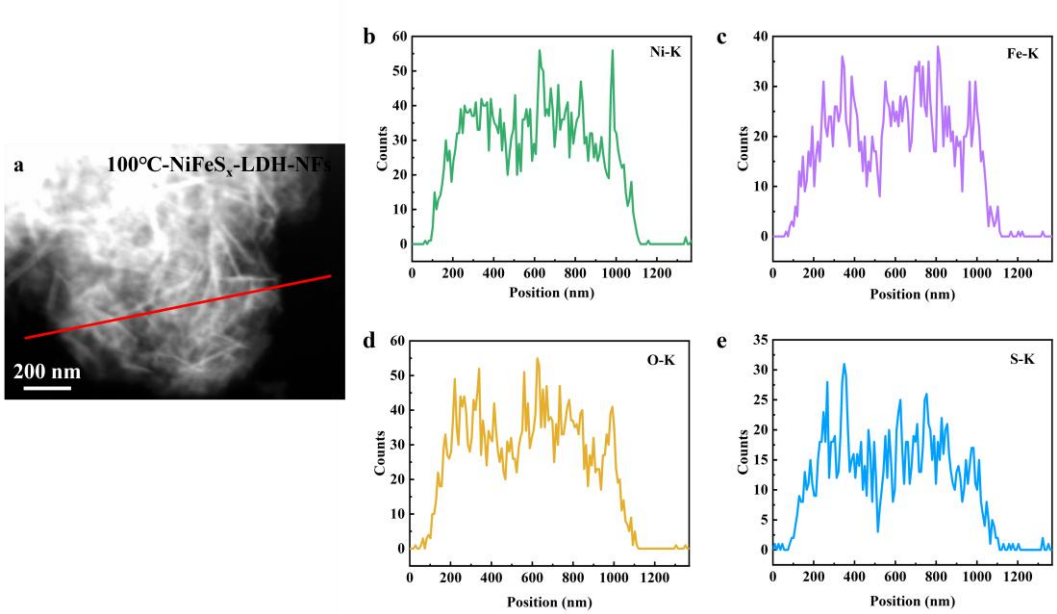

Fig. S8 STEM-EDS line scan images of 100 ℃-$NiFeS_x$-LDH-NFs.

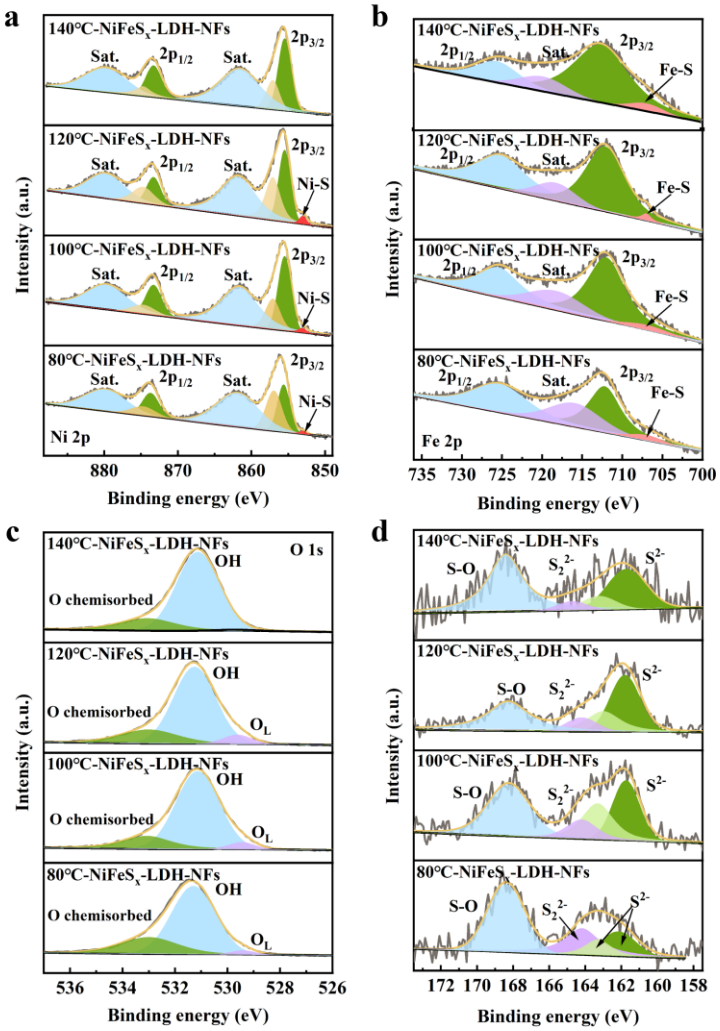

Fig. S9 X-ray photoelectron spectroscopy (XPS) spectra of $NiFeS_x$-LDH-NFs synthesized by hydrothermal at different temperatures: High-resolution XPS spectra of (a) Ni 2p, (b) Fe 2p, (c) O 1s and (d) S 2p.

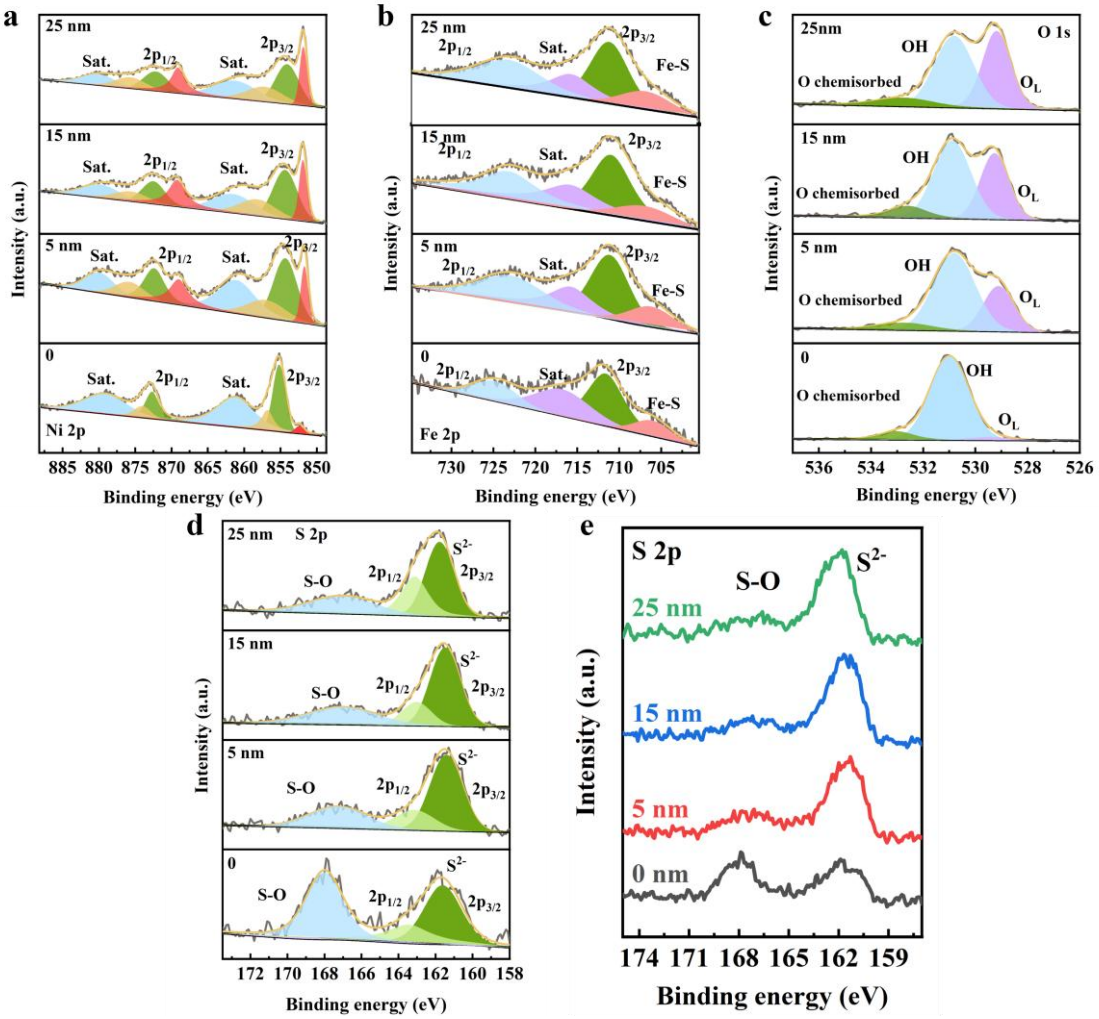

Fig. S10 Depth profile XPS spectra of $NiFeS_x$-LDH-NFs. High-resolution spectra of (a) Ni 2p, (b) Fe 2p, (c) O 1s and (d) S 2p in different etching depth, (e) The comparison of peak intensities in the S 2p XPS spectra.

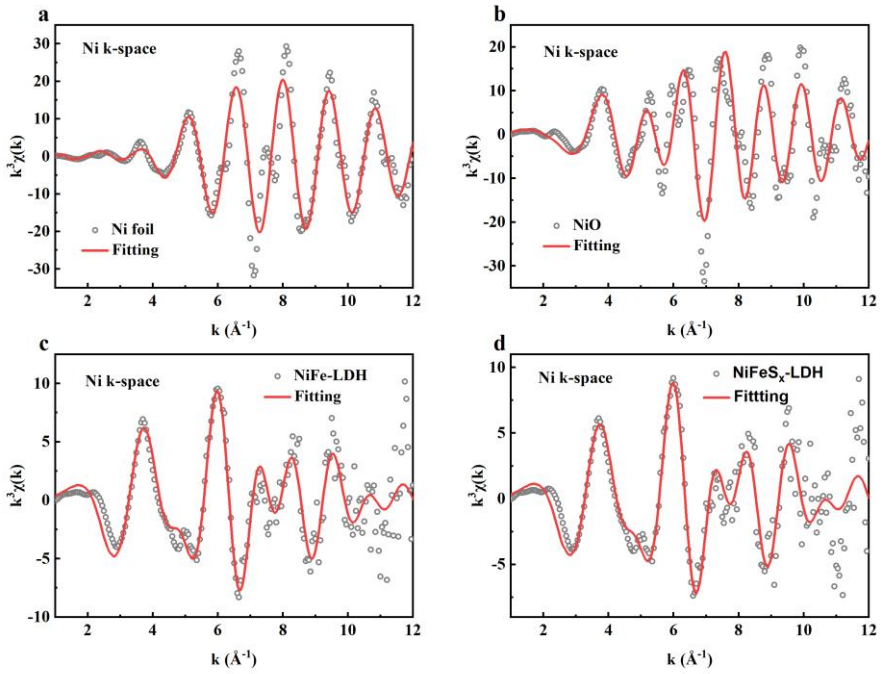

Fig. S11 Ni K-edge EXAFS (points) and the curvefit (line) for samples, shown in K^3 weighted k-space.

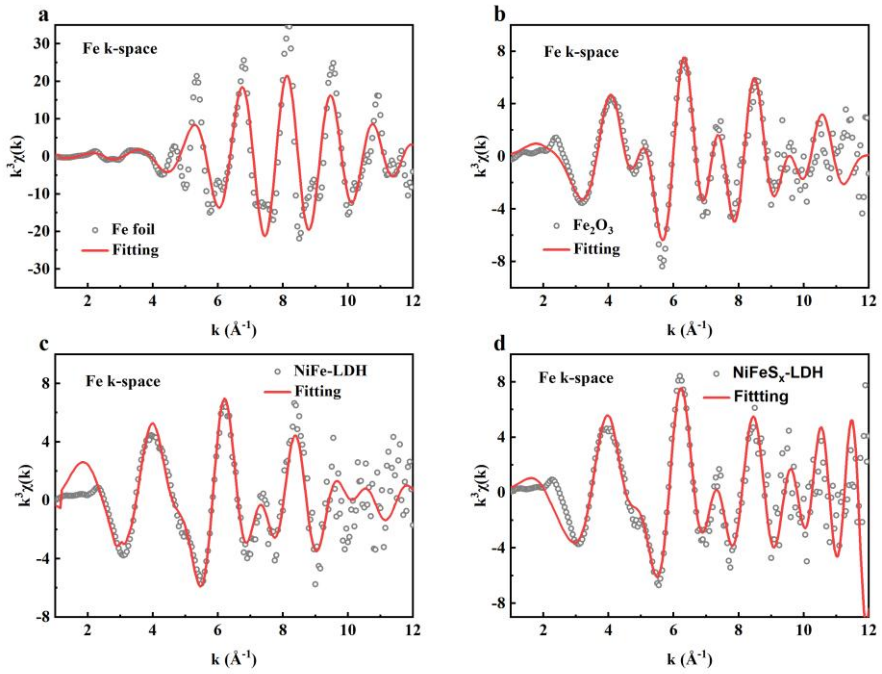

Fig. S12 Fe K-edge EXAFS (points) and the curvefit (line) for samples, shown in K^3 weighted k-space.

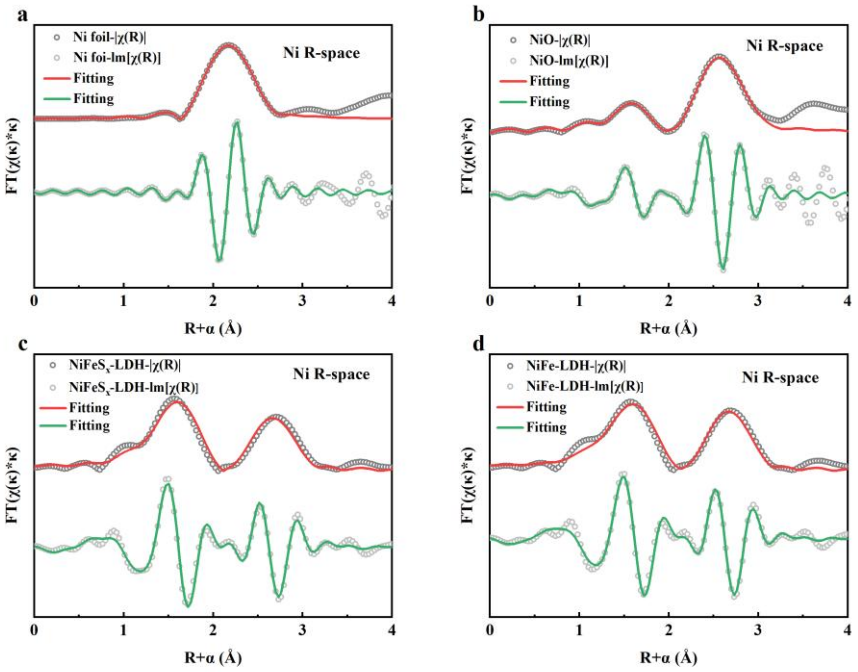

Fig. S13 Ni K-edge EXAFS (points) and curvefit (line) for samples, shown in R-space (FT magnitude and imaginary component). The data are K^3-weighted and not phase-corrected.

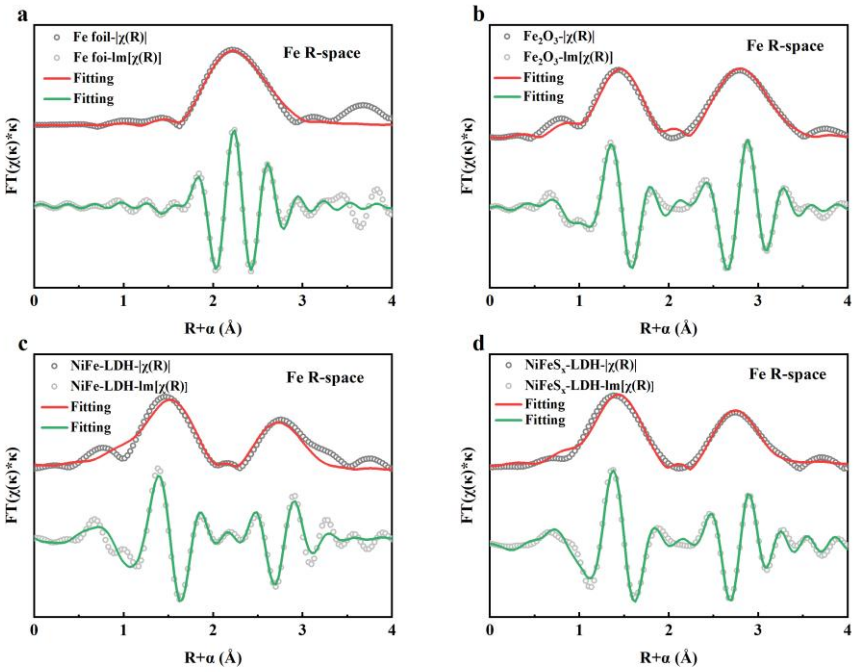

Fig. S14 Fe K-edge EXAFS (points) and curvefit (line) for samples, shown in R-space (FT magnitude and imaginary component). The data are K^3-weighted and not phase-corrected.

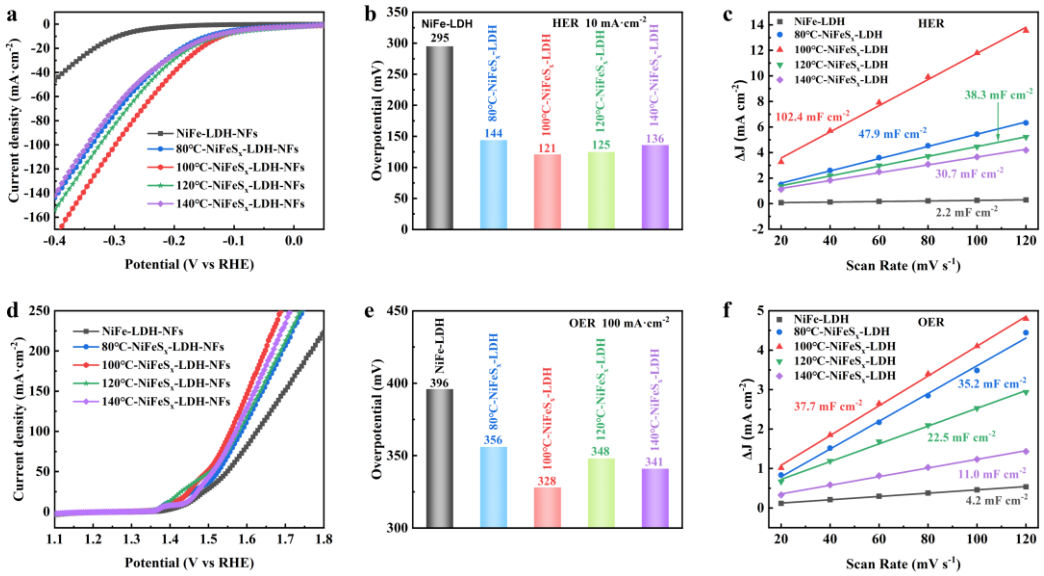

Fig. S15 Water Electrolysis performance of NiFe-LDH-NFs and $NiFeS_x$-LDH-NFs prepared at different reaction temperatures. (a) and (d) LSV curves for HER and OER (10 mV s^{-1}), respectively, (b) and (e) constant current overpotentials for HER and OER, respectively, (c) and (f) ECSA curves for HER and OER, respectively.

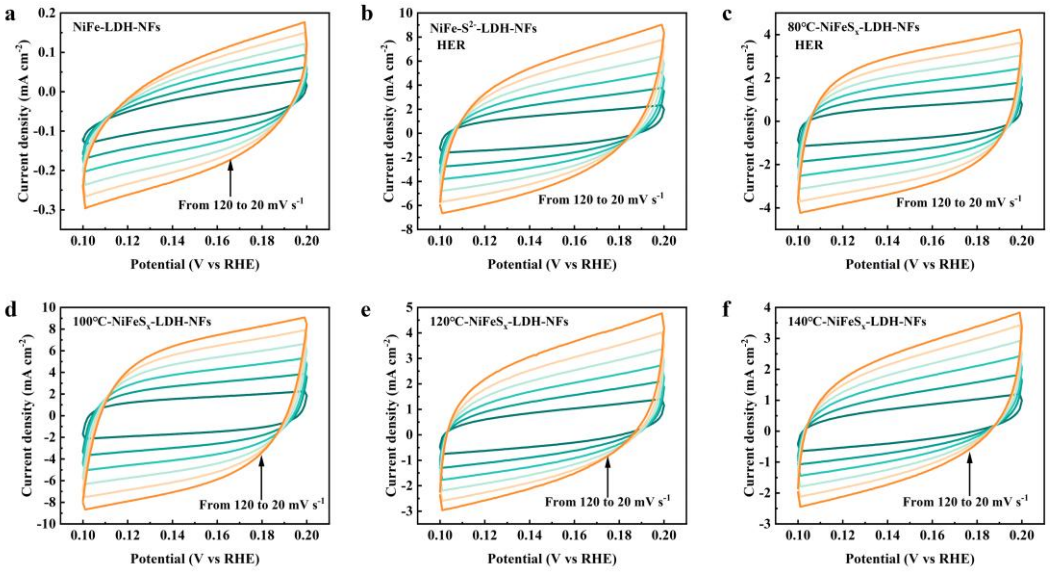

Fig. S16 CV curves for NiFe-LDH-NFs, NiFe-S^{2-}-LDH-NFs, and $NiFeS_x$-LDH-NFs prepared at different reaction temperatures for different scan rates in the voltage range of 0.1-0.2 V vs RHE.

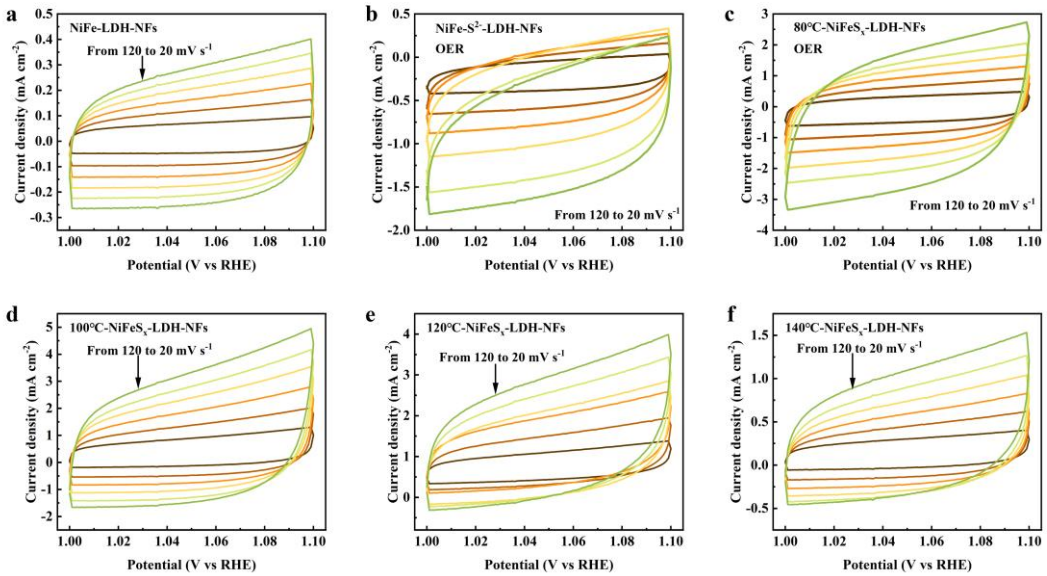

Fig. S17 CV curves for NiFe-LDH-NFs, NiFe-S^{2-}-LDH-NFs, and $NiFeS_x$-LDH-NFs prepared at different reaction temperatures for different scan rates in the voltage range of 1.0-1.1 V vs RHE.

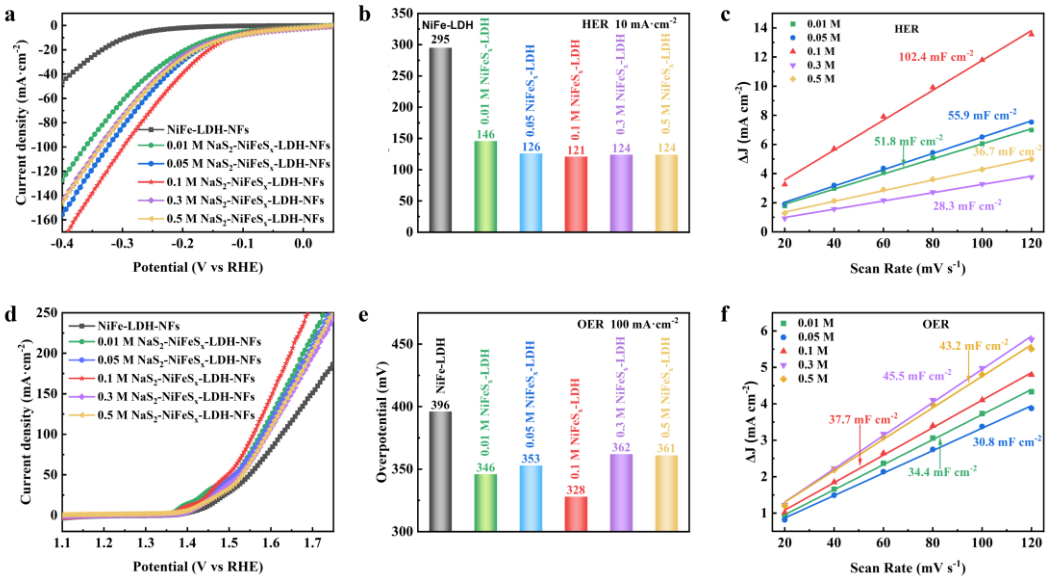

Fig. S18 Water Electrolysis performance of NiFe-LDH-NFs and $NiFeS_x$-LDH-NFs prepared by different concentrations of Na_2S. (a) and (d) LSV curves for HER and OER (10 mV s^{-1}), respectively, (b) and (e) constant current overpotentials for HER and OER, respectively, (c) and (f) ECSA curves for HER and OER, respectively.

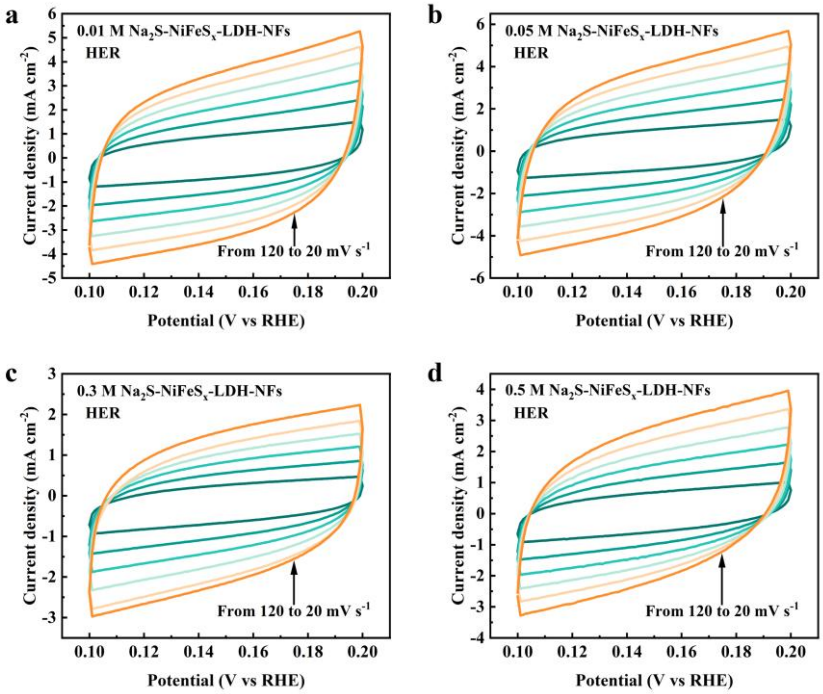

Fig. S19 CV curves for NiFe-LDH-NFs and $NiFeS_x$-LDH-NFs at different scan rates in the voltage range of 0.1-0.2 V vs RHE.

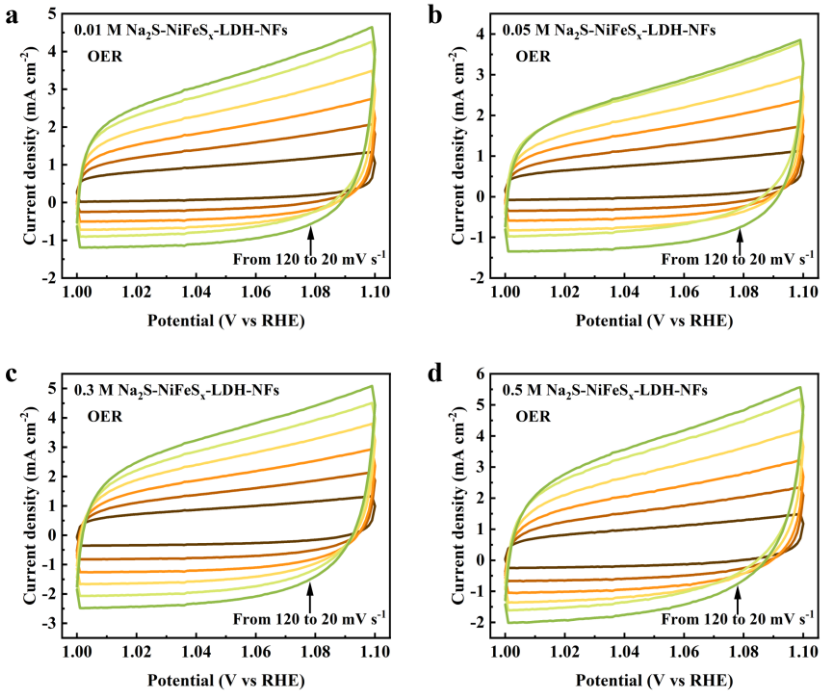

Fig. S20 CV curves for NiFe-LDH-NFs and $NiFeS_x$-LDH-NFs at different scan rates in the voltage range of 1.0-1.1 V vs RHE.

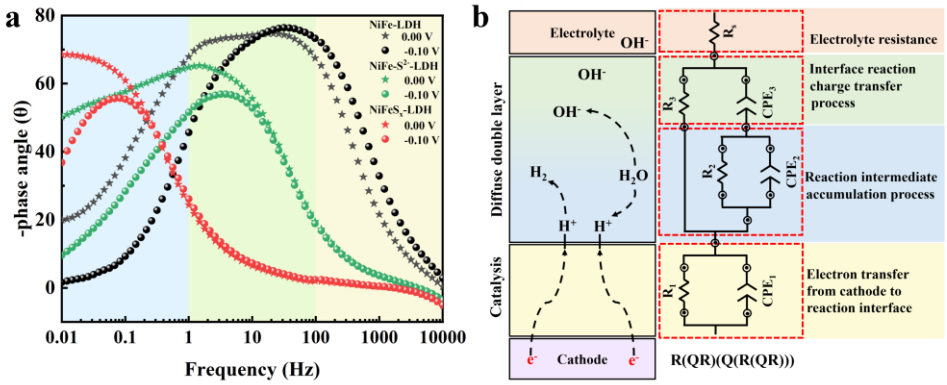

Fig. S21 (a) Comparison of EIS Bode plots in η= 0 mV and η= 100 mV for NiFe-LDH-NFs, NiFe-S^{2-}-LDH-NFs, and $NiFeS_x$-LDH-NFs, (b) Schematic diagram of electrode structure and equivalent circuit.

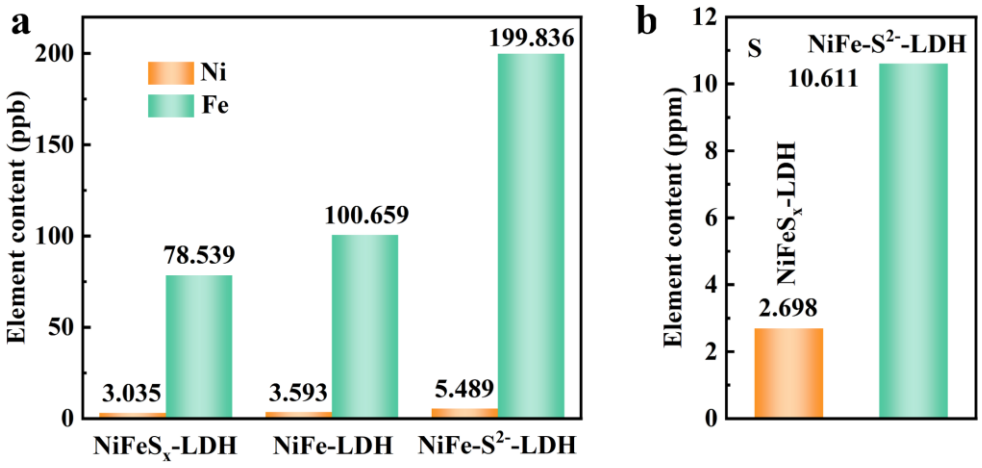

Fig. S22 The inductively coupled plasma optical emission spectroscopy (ICP-OES) test of the electrolyte after a 12-hour OER stability test conducted at a current density of 100 mA cm^{-2}: (a) content of nickel and iron elements, (b) content of sulfur element.

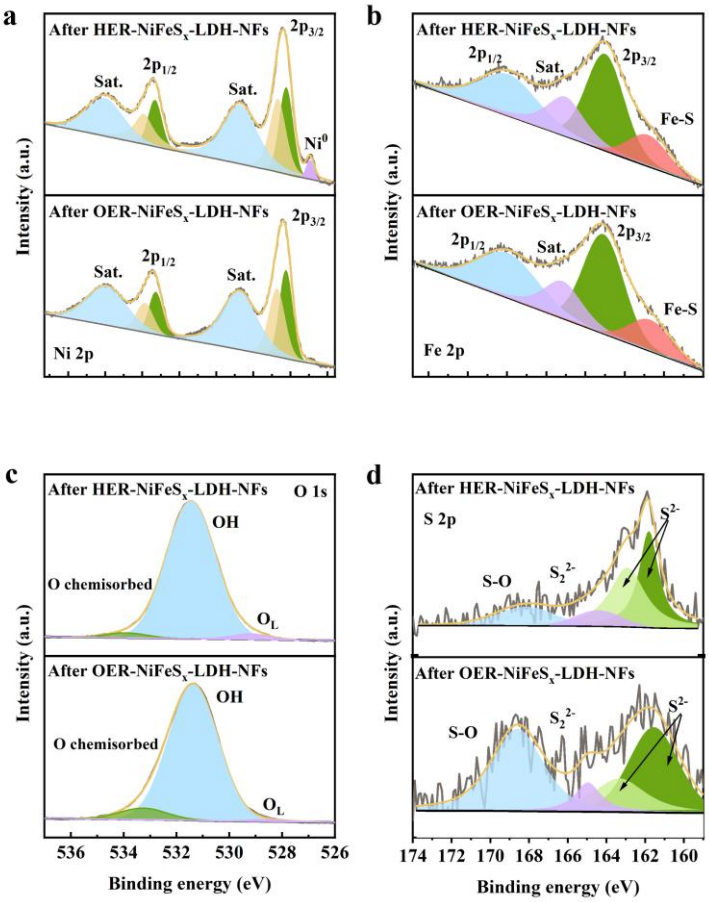

Fig. S23 The XPS spectra of $NiFeS_x$-LDH-NFs catalysts as cathode and anode after water splitting.

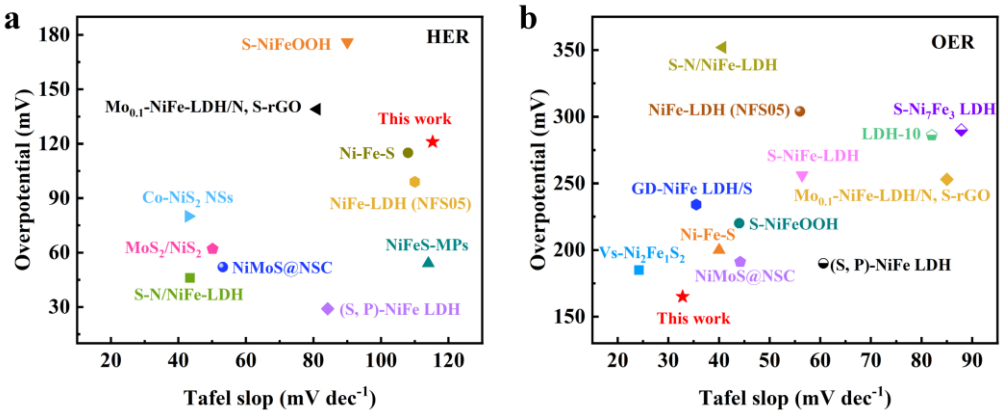

Fig. S24 (a) HER performance at 10 mA cm^{-2} compared to recently reported catalysts in 1 M KOH, (b) OER performance at 10 mA cm^{-2} compared to recently reported catalysts in 1 M KOH.

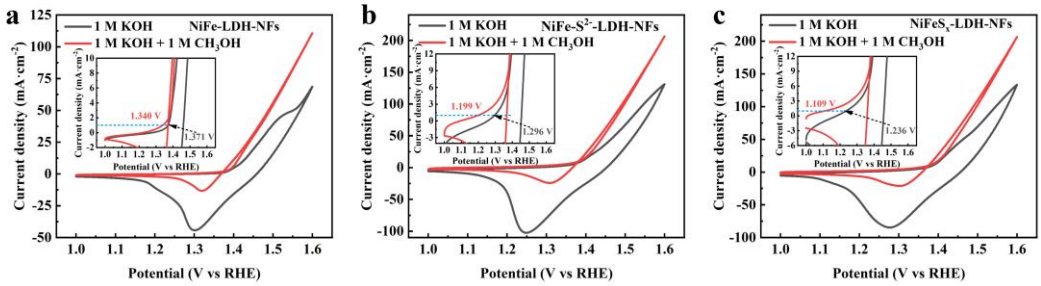

Fig. S25 CV curves of different samples in 1 M KOH with or without 1 M methanol: (a) NiFe-LDH-NFs, (b) NiFe-S^{2-}-LDH-NFs, and (c) $NiFeS_x$-LDH-NFs.

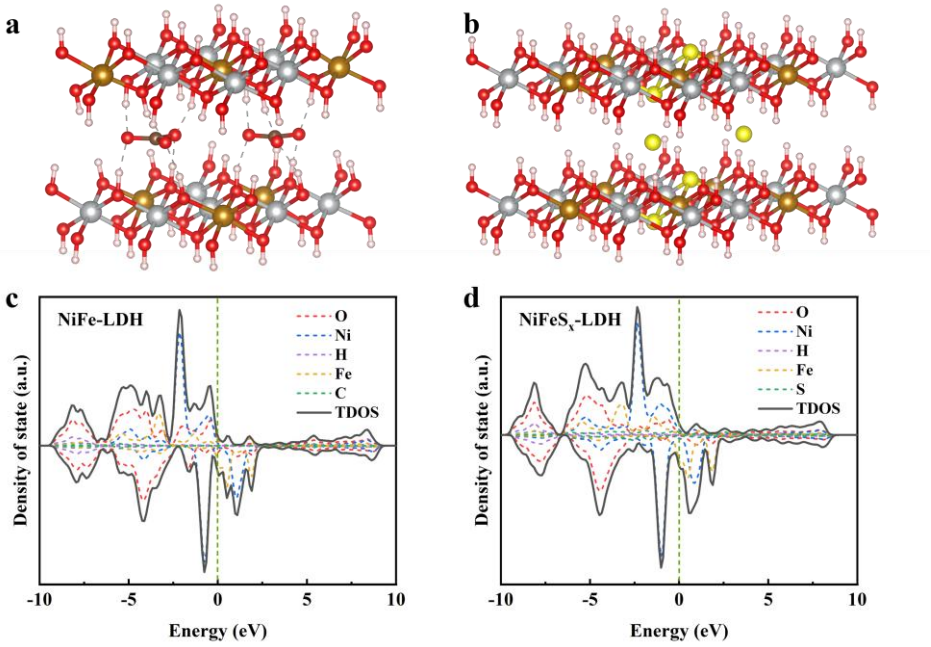

Fig. S26 (a) and (b) Structural models of NiFe LDH and $NiFeS_x$-LDH, (c) and (d) Density of state (DOS) for NiFe LDH and $NiFeS_x$-LDH.

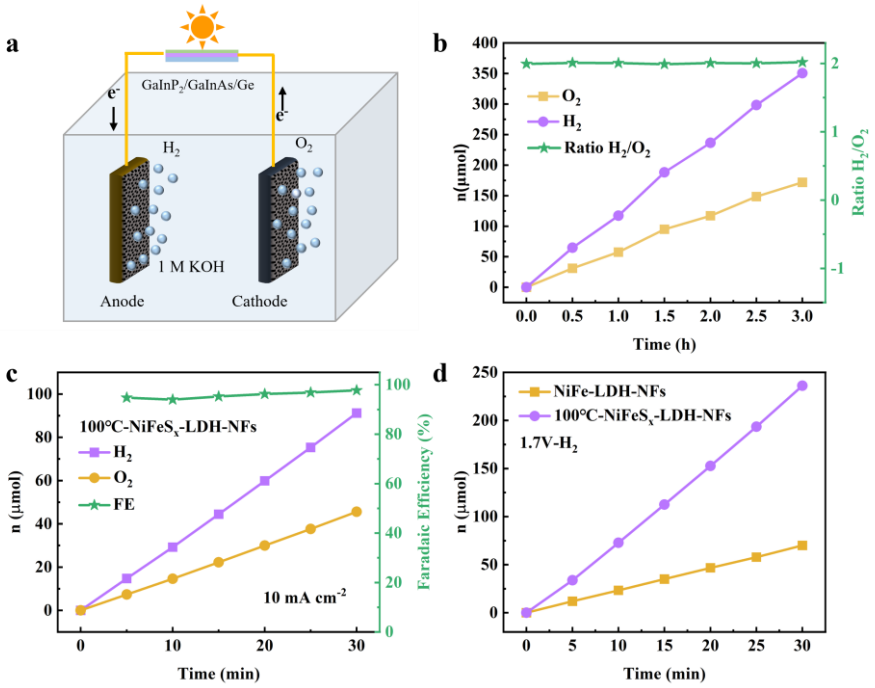

Fig. S27 The solar-driven alkaline water electrolysis performance. (a) PVE device schematic, (b) Hydrogen-to-oxygen ratio of the PVE system, (c) FE test at 10 mA cm^{-2}, (d) Comparison of hydrogen evolution of $NiFeS_x$-LDH-NFs and NiFe-LDH-NFs at 1.7 V.

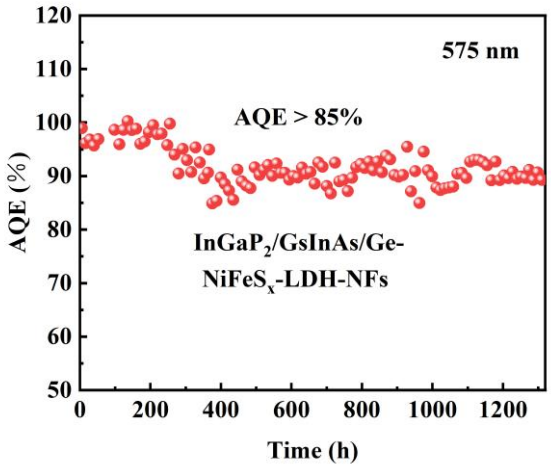

Fig. S28 Apparent quantum efficiency (AQE) PVE H_2 evolution by $GaInP_2$/InGaAs/Ge-$NiFeS_x$-LDH-NFs at 575 nm.

3. Supporting tables

Table S1

Samples	$2\theta_{(003)}$ (°)	Basal spacings (Å)
NiFe-LDH	11.642	7.595
NiFe-S^{2-}-LDH	11.614	7.613
$NiFeS_x$-LDH	11.432	7.734

Table S2 Ni K-edge EXAFS curve fitting parameters

	shell	CN	R(Å)	σ^2(Å^2)	ΔE_0(eV)	R factor
Ni-foil	Ni-Ni	12	2.48±0.002	0.0061	6.80	0.0006
NiO	Ni-O	6	2.07±0.01	0.0082	-3.00	0.004
	Ni-Ni	12	2.96±0.007	0.0081		
NiFe-LDH	Ni-O	6	2.06±0.011	0.0099	-1.96	0.012
	Ni-Fe	3	3.09±0.013	0.0109		
$NiFeS_x$-LDH	Ni-S/O	6	2.05±0.008	0.0078	-3.08	0.011
	Ni-Fe	3	3.09±0.011	0.0101		

EXAFS fitting parameters at the Ni K-edge for various samples（S_0^2 = 0.78 from Ni-foil）CN: coordination numbers; R: bond distance; σ^2: Debye-Waller factors; ΔE_0: the inner potential correction; R factor: goodness of fit. Error bounds that characterize the structural parameters obtained by EXAFS spectroscopy were estimated as CN ± 20%; R ± 1%; σ^2 ± 20%.

Table S3 Fe K-edge EXAFS curve fitting parameters

	shell	CN	R(Å)	σ^2(Å^2)	ΔE_0(eV)	R factor
Fe-foil	Fe-Fe	8	2.47±0.02	0.0079	5.0	0.017
	Fe-Fe	4	2.84±0.02	0.0030		
Fe_2O_3	Fe-O	3	1.94±0.01	0.0044	-4.8	0.010
	Fe-Fe	3	3.40±0.08	0.0116		
NiFe-LDH	Fe-O	6	2.02±0.02	0.0099	5.3	0.021
	Fe-Ni	6	3.11±0.03	0.0133		
$NiFeS_x$-LDH	Fe-S/O	6	1.95±0.01	0.0089	-8.0	0.009
	Fe-Ni	6	3.22±0.03	0.0118		

EXAFS fitting parameters at the Fe K-edge for various samples（S_0^2 = 0.98 from Fe-foil）CN: coordination numbers; R: bond distance; σ^2: Debye-Waller factors; ΔE_0: the inner potential correction; R factor: goodness of fit. Error bounds that characterize the structural parameters obtained by EXAFS spectroscopy were estimated as CN ± 20%; R ± 1%; σ^2 ± 20%.

Table S4 Optimum impedance fit parameters for NiFe-LDH-NFs during HER in 1 M KOH.

E (V vs. RHE)	R_s	CPE_1T	CPE_1P	R_1	CPE_2T	CPE_2P	R_2	CPE_3T	CPE_3P	R_3
+0.05	0.927	0.0019	1.123	3.56	0.0013	0.912	533.3	0.0027	0.855	7463
0.00	0.925	0.0027	1.099	3.46	0.0019	0.891	615	0.002	0.917	1501
-0.05	0.945	0.0018	1.190	3.40	0.0018	0.888	433.2	0.0009	0.914	824.5
-0.10	0.946	0.0019	1.146	3.17	0.0024	0.890	324.2	0.0006	0.92	478.3
-0.15	0.946	0.0024	1.080	3.08	0.0052	1.711	307.9	0.0004	0.929	265.5
-0.20	0.944	0.0017	0.960	2.34	0.0009	0.878	80.37	0.0002	1.139	150
-0.25	0.950	0.0022	0.884	2.40	0.0011	0.886	29.64	0.0001	1.122	79.85

Table S5 Optimum impedance fit parameters for NiFe-S^{2-}-LDH-NFs during HER in 1 M KOH.

E (V vs. RHE)	R_s	CPE_1T	CPE_1P	R_1	CPE_2T	CPE_2P	R_2	CPE_3T	CPE_3P	R_3
+0.05	0.843	0.062	1.124	1.493	0.035	0.801	49.01	0.023	0.825	1581
0.00	0.840	0.086	1.107	1.347	0.036	0.791	43.46	0.027	0.813	944.4
-0.05	0.838	0.088	1.066	1.283	0.040	0.793	30.27	0.029	0.797	248.5
-0.10	0.841	0.065	1.044	1.238	0.038	0.788	27.82	0.031	0.808	60.52
-0.15	0.844	0.042	0.996	1.115	0.053	0.924	9.546	0.029	0.758	16.30
-0.20	0.849	0.710	0.533	1.035	0.166	1.051	6.126	0.020	0.822	5.18
-0.25	0.858	7.14×10^{11}	9.240	0.400	0.032	1.168	4.650	0.031	0.758	2.61

Table S6 Optimum impedance fit parameters for $NiFeS_x$-LDH-NFs during HER in 1 M KOH.

E (V vs. RHE)	R_s	CPE_1T	CPE_1P	R_1	CPE_2T	CPE_2P	R_2	CPE_3T	CPE_3P	R_3
+0.05	0.707	0.928	0.539	0.321	0.456	0.870	9.99×10^{19}	34.39	0.18	554
0.00	0.711	1.001	0.503	0.321	0.487	0.846	395.7	20.06	0.781	471.4
-0.05	0.712	0.973	0.501	0.306	0.469	0.833	269.8	22864	0.246	183.2
-0.10	0.714	0.983	0.484	0.267	0.586	0.885	145.8	1.333	0.681	29.28
-0.15	0.717	0.774	0.509	0.175	1.444	1.196	13.95	0.405	0.762	6.061
-0.20	0.721	0.472	0.561	0.161	0.317	0.805	15.56	0.511	1.542	1.823
-0.25	0.726	0.285	0.624	0.142	0.430	0.794	1.312	0.232	1.204	0.981

Table S7 Electrochemical impedance fit parameters of OER for three samples, NiFe-LDH-NFs, NiFe-S^{2-}-LDH-NFs, and $NiFeS_x$-LDH-NFs, in 1 M KOH.

Samples	R_s	CPE_1T	CPE_1P	R_1
NiFe-LDH-NFs	0.980	1.183	0.898	20.98
NiFe-S^{2-}-LDH-NFs	0.726	1.087	0.883	13.82
$NiFeS_x$-LDH-NFs	0.773	1.645	0.833	7.61

Table S8 Comparison of the electrocatalytic HER activity for NiFe-S^{2-}-LDH-NFs, $NiFeS_x$-LDH-NFs, and reported nonprecious catalysts in 1.0 M KOH.

Catalysis	Substrate	η_{10} (mV)	Tafel slope (mV dec^{-1})	Ref.
NiFe-S^{2-}-LDH	**Ni foam**	**149**	**117.5**	**This work**
$NiFeS_x$-LDH	**Ni foam**	**121**	**115.3**	**This work**
S-N/NiFe-LDH	Ni foam	46	43.4	[4]
(S, P)-NiFe LDH	Ni Fe foam	29	84.2	[5]
NiFe-LDH (NFS05)	Ni foam	99	110	[6]
S-NiFe-LDH	NiFe foam	171	174.9	[7]
NiFeS-MPs	Ni foam	54	114	[8]
S-NiFeOOH	Ni foam	176	90	[9]
$Mo_{0.1}$-NiFe-LDH/N, S-rGO	Ni foam	139	81	[10]
NiMoS@NSC	Ni foam	52	53.14	[11]
MoS_2/NiS_2	carbon cloth	62	50.1	[12]
Ni-Fe-S	carbon paper	115	108	[13]
Co-NiS_2 NSs	Ni foam	80	43	[14]

Table S9 Comparison of the electrocatalytic OER activity for NiFe-S^{2-}-LDH-NFs, $NiFeS_x$-LDH-NFs, and reported nonprecious catalysts in 1.0 M KOH.

Catalysis	Substrate	η_{10} (mV)	Tafel slope (mV dec^{-1})	Ref.
NiFe-S^{2-}-LDH	**Ni foam**	**203**	**68.6**	**This work**
$NiFeS_x$-LDH	**Ni foam**	**165**	**32.8**	**This work**
S-N/NiFe-LDH	Ni foam	352	40.7	[4]
S-NiFe-LDH	Ni foam	220	41.3	[15]
Ni-Fe-S	Ni foam	200	40	[16]
S-Ni_7Fe_3 LDH	graphite felt	290	87.84	[17]
Vs-$Ni_2Fe_1S_2$	Ni foam	185	24.18	[18]
(S, P)-NiFe LDH	Ni Fe foam	190	60.6	[5]
GD-NiFe LDH/S	Ni foam	234	35.5	[19]
NiFe-LDH (NFS05)	Ni foam	304	56	[6]
S-NiFe-LDH	NiFe foam	256	56.4	[7]
S-NiFeOOH	Ni foam	220	44	[9]
LDH-10	glass carbon	286	82	[20]
$Mo_{0.1}$-NiFe-LDH/N, S-rGO	Ni foam	253	85	[10]
NiMoS@NSC	Ni foam	191	44.18	[11]

References

1. G. Kresse and J. Furthmüller, *Physical Review B*, 1996, **54**, 11169-11186.
2. J. P. Perdew, K. Burke and M. Ernzerhof, *Phys. Rev. Lett.*, 1996, **77**, 3865-3868.
3. J. K. Nørskov, J. Rossmeisl, A. Logadottir, L. Lindqvist, J. R. Kitchin, T. Bligaard and H. Jónsson, *The Journal of Physical Chemistry B*, 2004, **108**, 17886-17892.
4. C. Lai, Z. Guo, L. Nie, D. Zhang, F. Li and S. Ji, *J. Electroanal. Chem.*, 2023, **944**, 117640.
5. G. Yang, W. Peng, J. Ye, R. Hu, Q. Han, S. Li and B. Yuan, *J. Alloys Compd.*, 2025, **1017**, 179074.
6. T. Susikumar, P. J. Jesuraj, M. Navaneethan, A. D. Savariraj, C. M. Lee and S. Y. Ryu, *Surf. Interfaces*, 2024, **55**, 105448.
7. S. Zhang, Y. Ji, S. Wang, P. Zhang, D. Shi, F. Lu and B. Zhang, *J. Alloys Compd.*, 2024, **1002**, 175323.
8. J. Choi, A. Nkhama, A. Kumar, S. R. Mishra, F. Perez and R. K. Gupta, *Int. J. Hydrogen Energy*, 2022, **47**, 7511-7521.
9. C. Kim, S. H. Kim, S. Lee, I. Kwon, S. H. Kim, S. Kim, C. Seok, Y. S. Park and Y. Kim, *J. Energy Chem.*, 2022, **64**, 364-371.
10. K. R. Kumar, N. D. Sri, V. N. Kale and T. Maiyalagan, *Int. J. Hydrogen Energy*, 2025, **101**, 837-847.
11. X. Fan, B. Li, C. Zhu, F. Yan, X. Zhang and Y. Chen, *Small*, 2024, **20**, 2309655.
12. J. Lin, P. Wang, H. Wang, C. Li, X. Si, J. Qi, J. Cao, Z. Zhong, W. Fei and J. Feng, *Adv. Sci.*, 2019, **6**, 1900246.
13. Z. Yin, S. Zhang, J. Li, S. Ma, W. Chen, X. Ma, Y. Zhou, Z. Zhang and X. Wang, *New J. Chem.*, 2021, **45**, 12996-13003.
14. J. Yin, J. Jin, H. Zhang, M. Lu, Y. Peng, B. Huang, P. Xi and C.-H. Yan, *Angew. Chem. Int. Ed.*, 2019, **58**, 18676-18682.
15. J. Long, J. Zhang, L. Li, Y. Wen, X. Xu and F. Wang, *Int. J. Hydrogen Energy*, 2024, **90**, 1424-1434.
16. C. Xuan, W. Lei, J. Wang, T. Zhao, C. Lai, Y. Zhu, Y. Sun and D. Wang, *J. Mater. Chem. A*, 2019, **7**, 12350-12357.
17. D. Li, M. U. Mushtaq, Y. Tang, S. Li, F. Hou, K. S. Ayub, L. Cao and J. Yang, *Res. Chem. Intermed.*, 2025, **51**, 3019-3038.
18. Z. Wang, S. Liu, Y. Ma, J. Guo, B. Xin, C. Wang, C. Wang and J. Tong, *J. Energy Chem.*, 2025, **105**, 872-884.
19. J. Zhang, Q. Chen, P. Zhao, A. Cai, X. Fan, W. Peng and Y. Li, *Small*, 2025, **21**, 2409265.
20. C.-X. Zhao, B.-Q. Li, M. Zhao, J.-N. Liu, L.-D. Zhao, X. Chen and Q. Zhang, *Energy Environ. Sci.*, 2020, **13**, 1711-1716.